nature COMMUNICATIONS

ARTICLE

https://doi.org/10.1038/s41467-021-23381-9 OPEN

Dynamic fingerprint of fractionalized excitations in single-crystalline $Cu_3Zn(OH)_6FBr$

Ying Fu[1,8], Miao-Ling Lin[2,3,8], Le Wang[1], Qiye Liu[1], Lianglong Huang[1], Wenrui Jiang[1], Zhanyang Hao[1], Cai Liu[1], Hu Zhang[4], Xingqiang Shi[4], Jun Zhang[2,3,5], Junfeng Dai[1], Dapeng Yu[1], Fei Ye[1,6], Patrick A. Lee[7], Ping-Heng Tan[2,3,5]✉ & Jia-Wei Mei[1,6]✉

Beyond the absence of long-range magnetic orders, the most prominent feature of the elusive quantum spin liquid (QSL) state is the existence of fractionalized spin excitations, i.e., spinons. When the system orders, the spin-wave excitation appears as the bound state of the spinon-antispinon pair. Although scarcely reported, a direct comparison between similar compounds illustrates the evolution from spinon to magnon. Here, we perform the Raman scattering on single crystals of two quantum kagome antiferromagnets, of which one is the kagome QSL candidate $Cu_3Zn(OH)_6FBr$, and another is an antiferromagnetically ordered compound $EuCu_3(OH)_6Cl_3$. In $Cu_3Zn(OH)_6FBr$, we identify a unique one spinon-antispinon pair component in the E_{2g} magnetic Raman continuum, providing strong evidence for deconfined spinon excitations. In contrast, a sharp magnon peak emerges from the one-pair spinon continuum in the E_g magnetic Raman response once $EuCu_3(OH)_6Cl_3$ undergoes the antiferromagnetic order transition. From the comparative Raman studies, we can regard the magnon mode as the spinon-antispinon bound state, and the spinon confinement drives the magnetic ordering.

[1] Shenzhen Institute for Quantum Science and Engineering, and Department of Physics, Southern University of Science and Technology, Shenzhen, China. [2] State Key Laboratory of Superlattices and Microstructures, Institute of Semiconductors, Chinese Academy of Sciences, Beijing, China. [3] Center of Materials Science and Optoelectronics Engineering & CAS Center of Excellence in Topological Quantum Computation, University of Chinese Academy of Sciences, Beijing, China. [4] College of Physics Science and Technology, Hebei University, Baoding, China. [5] Beijing Academy of Quantum Information Science, Beijing, China. [6] Shenzhen Key Laboratory of Advanced Quantum Functional Materials and Devices, Southern University of Science and Technology, Shenzhen, China. [7] Department of Physics, Massachusetts Institute of Technology, Cambridge, MA, USA. [8] These authors contributed equally: Ying Fu, Miao-Ling Lin. ✉email: phtan@semi.ac.cn; meijw@sustech.edu.cn

Quantum spin liquid (QSL) represents a new class of condensed matter states characterized by the long-range many-body entanglement of topological orders[1–9]. The lattice of the spin-1/2 kagome network is a long-sought platform for antiferromagnetically interacting spins to host a QSL ground state[10–16]. However, a structurally ideal realization of the kagome lattice in experiments is rare. Herbersmithite [$ZnCu_3(OH)_6Cl_2$] is the first promising kagome QSL candidate[3,16–23], in which no long-range magnetic order was detected down to low temperature[17,18], and inelastic neutron scattering revealed a magnetic continuum, as a hallmark of fractionalized spin excitations[20,22]. Up to date, most, if not all, experimental information on the nature of kagome QSL relies on a single compound of Herbertsmithite. Considering the fact that a lattice distortion has recently been confirmed in Herbersmithite[24,25], which stimulates investigations on the subtle magneto-elastic effect in the kagome materials[26,27], an alternative realization of the QSL compound with the ideal kagome lattice is still in urgent need. Zn-Barlowite [$Cu_3Zn(OH)_6FBr$] is another candidate for a kagome QSL ground state[28–38] with no lattice distortion being reported yet. Measurements on the powder samples didn't detect the long-range magnetic order down to temperatures of 0.02 K, four orders of magnitude lower than the Curie–Weiss temperature[30,32]. Besides the lack of magnetic order, the fractionalized spin excitations, i.e., spinons, is essential evidence for the long-range entanglement pattern in QSL. However, spectroscopic evidence for the deconfined spinon excitations in Zn-Barlowite is still lacking, in part due to unavailable single-crystal samples.

Raman scattering is sensitive to the local symmetries depending on the light polarization[39,40], and also capable of detecting magnetic excitations ranging from the spin-wave magnon excitation to deconfined spionons[41–50]. Raman scattering has previously been reported for Herbertsmithite and revealed the multiple spinon scattering process[19]. In recent years, the atacamite family $ReCu_3(OH)_6Cl_3$ (Re=Y, Eu, Sm, and Nd) with the perfect kagome lattice has been synthesized and a chiral 120° antiferromagnetic (AFM) order with the wave vector $\mathbf{q} = 0$ is identified in the ground state[51–55]. The kagome spin systems can be described by the kagome Heisenberg model with the Dzyaloshinski–Moriya (DM) interaction

$$H = J\sum_{\langle ij\rangle}(\mathbf{S}_i \cdot \mathbf{S}_j) + D\hat{z} \cdot \sum_{\langle ij\rangle}\mathbf{S}_i \times \mathbf{S}_j, \quad (1)$$

where summation runs over nearest-neighbor bonds $\langle ij\rangle$, and J and D are the nearest-neighbor exchange and the DM interaction constants, respectively, for the spins $S_{i,j}$ on the i- and j-th sites. We ignore the in-plane DM interactions regarding to the previous electron paramagnetic resonance measurements in the related kagome systems[55,56]. A DM interaction larger than the critical value of $(D/J)_c \sim 0.08$ induces a chiral 120° AFM order from the QSL state[57–59]. By the first-principle calculations (Supplementary Note 1), Zn-Barlowite and $EuCu_3(OH)_6Cl_3$ have D/J values of 0.05 and 0.3, resulting in QSL and AFM ground states, respectively, consistent with the experimental identification of the ground states[30,54]. While the elementary spin excitation of the kagome QSL is the deconfined spinon, the low energy excitation in the kagome AFM ordered states is the magnon. A direct comparison by the magnetic Raman scattering can reveal the evolution from deconfined spinons in Zn-Barlowite to magnons in $EuCu_3(OH)_6Cl_3$, but has not been performed yet.

In this work, we exclude the kagome lattice distortion by angle-resolved polarized Raman (ARPR) scattering and second-harmonic-generation (SHG), and reveal the spin dynamics of spinon excitations on the single-crystalline $Cu_{3.18}Zn_{0.82}(OH)_6FBr$. We observe a remarkable E_{2g} magnetic Raman continuum, which can be decomposed into one spinon–antispinon pair (one-pair (1P)) and two spinon–antispinon pair (two-pair (2P)) components of spinon excitations, in line with theoretical studies of the kagome QSL[60]. The one-pair continuum is unique, serving as the fingerprint of spinons. In a control experiment, beside the two-magnon (2M) magnetic Raman continuum, we probe a sharp one-magnon (1M) Raman peak in $EuCu_3(OH)_6Cl_3$ below the AFM transition temperature. The magnon peak emerges from the 1P continuum in the magnetic Raman scattering, can be regarded as the bound state of the spinon–antispinon excitations. As schematically summarized in Fig. 1, our comparative Raman study demonstrates the spinon deconfinement and confinement in the kagome QSL compound and ordered antiferromagnet, respectively. The AFM order transition can be thought to be driven by the spinon confinement.

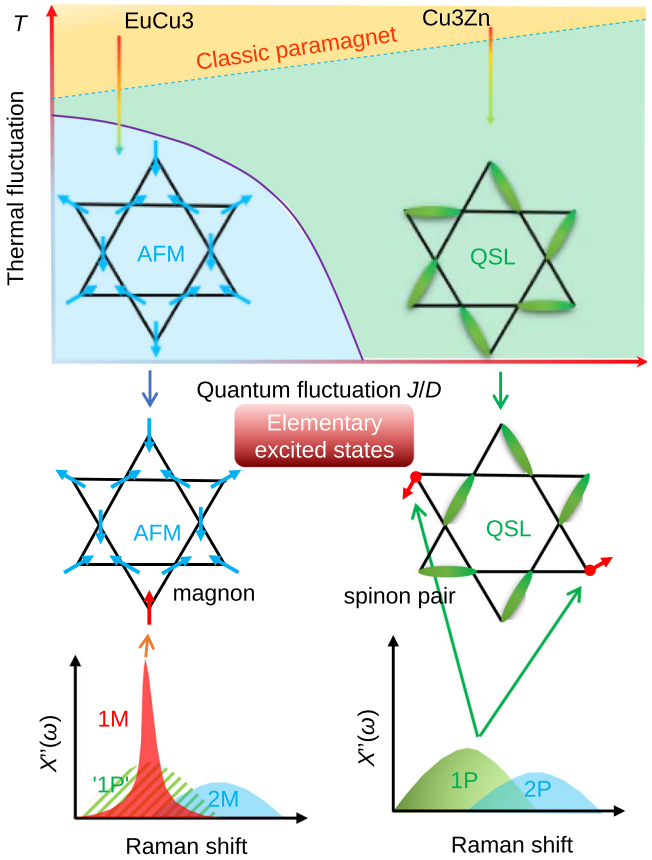

Fig. 1 Schematical comparative Raman responses for the AFM and QSL states. With a large DM interaction D, the kagome antiferromagnet develops a chiral 120° AFM ground state. Increasing J/D, the fluctuation of the kagome system increases, driving the system into the QSL state. By increasing the temperature, the thermal fluctuation melts the magnetic order and turns the system into the classic paramagnetic state at high temperatures. Cu_3Zn and $EuCu_3$ have the QSL and AFM ground states, and allow spinon and magnon excitations, respectively. Magnetic Raman scattering measures different elementary excited states in the two different ground states. Here 1P and 2P denote the one-pair and two-pair spinon excitations, respectively. 1M and 2M in AFM ordered state denote the one- and two-magnon excitations, respectively. The 1M Raman peak in AFM measures the magnon while the 1P Raman continuum in QSL probes the spinon excitations. The shadow background of the 1M peak, marked as `1P', denotes the continuum above T_N in $EuCu_3$, mimicking the 1P continuum in the QSL state.

Results

We grown single crystals of Barlowite $Cu_4(OH)_6FBr$, Zn-Barlowite $Cu_{3.18}Zn_{0.82}(OH)_6FBr$, and $EuCu_3(OH)_6Cl_3$ (we use the short-hand notation Cu_4, Cu_3Zn, and $EuCu_3$, respectively) with high quality ("Methods" and Supplementary Note 2). The interlayer Cu^{2+} concentration (18%) is comparable to that (15%) in Herbertsmithite[61]. We estimate the superexchange strength for the kagome spins in Cu_3Zn as $J \simeq 13$ meV by the Curie–Weiss temperature $\Theta_{CW} = -220$ K (Supplementary Note 2)[62]. The superexchange interaction for $EuCu_3$ is about $J \simeq 7$ meV[53–55]. Note the electronic ground state of Eu^{3+} in $EuCu_3$ is the non-magnetic $^7F_0$ configuration.

Figure 2a presents the temperature evolution of Raman spectra in Cu_3Zn with sharp phonon modes superimposing on the magnetic continuum background. With the help of first-principles calculations, we assign the symmetry representations for phonon modes in Supplementary Note 3. No structural phase transition is observed in Cu_3Zn down to 4 K. We tracked the Raman spectral evolution of the crystal structures from Cu_4 to Cu_3Zn (Supplementary Note 4). Cu_3Zn has no Raman-active mode related to the kagome Cu^{2+} vibrations, indicating the kagome layer remains intact. Cu_4 has distorted kagome layers at 200 K, signaled by an extra phonon mode at 62 cm^{-1} corresponding to the kagome Cu^{2+} vibration. The previous SHG study revealed the parity symmetry in Barlowite 2 [$Cu_4(OH)_6FBr$] and Zn-Barlowite [$Cu_{3.66}Zn_{0.33}(OH)_6FBr$][25]. We confirmed the inversion symmetry by SHG in our single crystals of Cu_3Zn (Supplementary Note 6).

Figures 2b–d are the ARPR responses of Cu_3Zn in three different polarization configurations ("Methods" and Supplementary Note 5). In the XX (XY) configuration, the incoming and outgoing light polarizations are parallel (perpendicular) and rotated simultaneously. In the X-only configuration, the outgoing polarization is fixed and only incoming light is rotated. Theoretically, the Raman cross section of a Kagome QSL ground state does not depend on the polarization of the incoming or outgoing light[39] and keeps invariant against rotating light polarization in the XX, XY, and X-only configurations. Figure 2b is the ARPR response for the magnetic continua at low frequency with the integrated Raman susceptibility $\chi' = \frac{2}{\pi}\int_{10cm^{-1}}^{60cm^{-1}} \frac{\chi''(\omega)}{\omega} d\omega$, where the susceptibility is related to the Raman intensity $I(\omega) = (1 + n(\omega))\chi''(\omega)$ with the bosonic temperature factor $n(\omega)$. Figure 2c and d are the corresponding results of the $Br^{-}E_{2g}$ phonon, and $O^{2-}A_{1g}$ phonon modes, respectively. For threefold rotation symmetry, the A_{1g} mode response follows the $\cos^2(\theta)$ function of the rotation angle θ in X-only configuration, keeps constant in XX polarization, and vanishes in XY configuration; the E_{2g} mode is isotropic in all the three configurations. The magnetic continuum contains both A_{1g} and E_{2g} channels at high temperature (290 K), and only the E_{2g} channel at low temperature (4 K). The experimental ARPR responses agree well with the theoretical dash-dotted curves, confirming the threefold rotational symmetry in the magnetic excitations (Fig. 2b) and lattice vibrations (Figs. 2c, d). We notice that in Herbertsmithite, although it was not discussed, the lattice distortion was evident by the anisotropic ARPR responses[19] and may account for the difference from our results.

Having established the structurally ideal realization of the kagome lattice by SHG and ARPR scattering, and the absence of the thermodynamic anomaly, we now present our spectroscopic results of spin dynamics in Cu_3Zn with subtracting phonon contributions. Figure 3a–c are the magnetic continuum of Cu_3Zn in the A_{1g} channel, which is activated only at high temperatures, and disappears at low temperatures. The integrated Raman susceptibility in Fig. 3b fits the thermally activated function, $\chi'(T) \propto e^{-\omega^*/T}$ with $\omega^* = 53$ cm^{-1}. The result suggests the A_{1g} continuum measures the thermal fluctuation of the interacting kagome

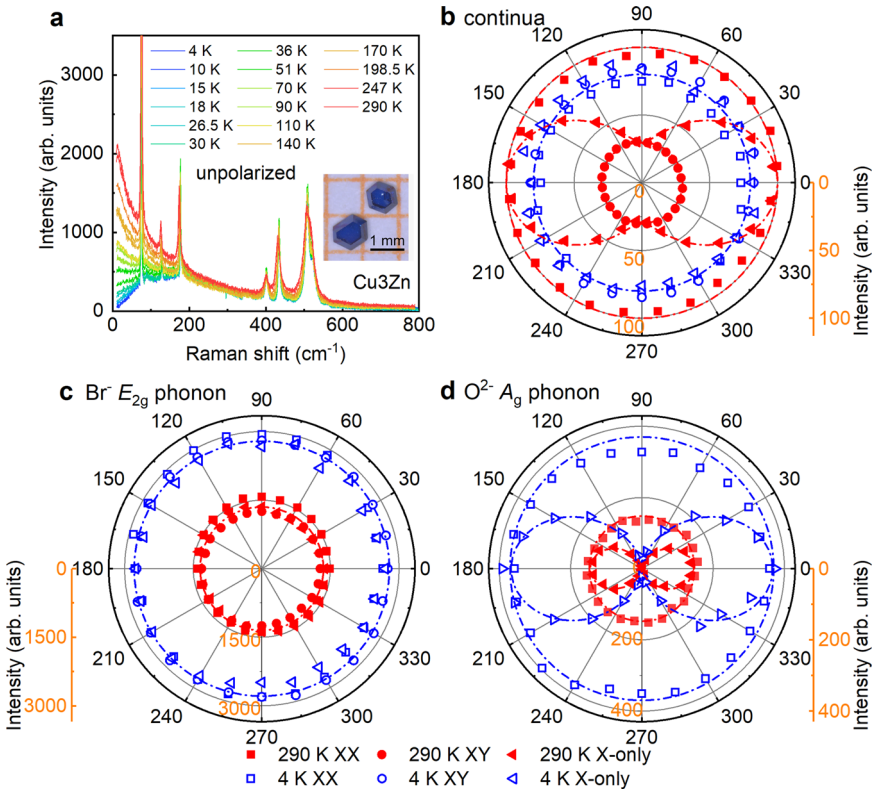

Fig. 2 Temperature dependent and ARPR spectra in Cu_3Zn. a Temperature evolution of unpolarized Raman spectra in Cu_3Zn. The inset is the photo of single crystals. ARPR intensity for low-energy continua (**b**), the $Br^{-}E_{2g}$ phonon (75 cm^{-1}) (**c**), and the $O^{2-}A_{1g}$ phonon (429 cm^{-1}) (**d**). The dash-dotted lines are the corresponding theoretical curves based on the C_3 rotation symmetry.

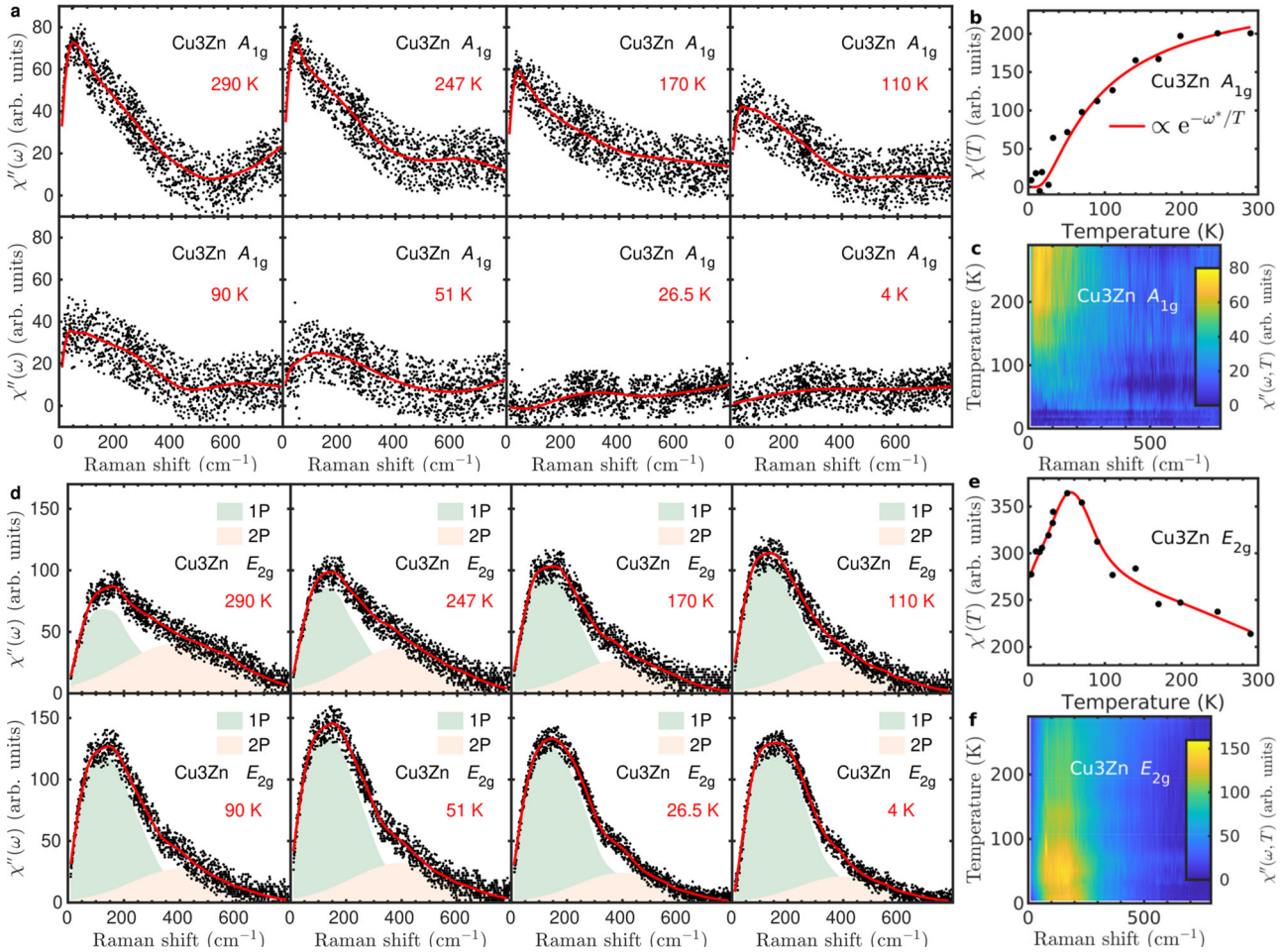

Fig. 3 Temperature dependent magnetic Raman continua in Cu_3Zn. a The A_{1g} Raman susceptibility $\chi''_{A_{1g}} = \chi''_{XX} - \chi''_{XY}$. The solid lines are guides to the eye. **b** Temperature dependence of the A_{1g} static Raman susceptibility $\chi'_{A_{1g}}(T) = \frac{2}{\pi}\int_{10\,\mathrm{cm}^{-1}}^{400\,\mathrm{cm}^{-1}} \frac{\chi''_{A_{1g}}(\omega)}{\omega} d\omega$. The solid line is a thermally activated function. **c** Color map of $\chi''_{A_{1g}}(\omega, T)$. **d** The E_{2g} Raman response function $\chi''_{E_{2g}} = \chi'_{XY}$. The solid lines are guides to the eye. The light green and pink shadow marked as "1P" and "2P" represent the one-pair and two-pair components of Raman continuum. **e** Temperature dependence of the E_{2g} static Raman susceptibility $\chi'_{E_{2g}}(T) = \frac{2}{\pi}\int_{10\,\mathrm{cm}^{-1}}^{780\,\mathrm{cm}^{-1}} \frac{\chi''_{E_{2g}}(\omega)}{\omega} d\omega$. The solid line is a guide to the eye. **f** Color map of $\chi''_{E_{2g}}(\omega, T)$.

spins[41,63,64]. Different from the A_{1g} channel, the pronounced E_{2g} magnetic Raman continuum persists down to 4 K (Fig. 3d–f), indicating the intrinsic quantum fluctuation of the kagome spins. The substantial low energy component has a non-monotonic temperature dependence. It increases with the temperature decreasing from 290 K to 50 K, but decreases with further temperature reducing as shown in Fig. 3d–f. The E_{2g} magnetic Raman susceptibility $\chi''(\omega, T)$ distributes the main spectral weight among the frequency region less than 400 cm^{-1}, and reaches the maximum at around 150 cm^{-1} and 50 K, as shown in Fig. 3f.

The low-energy E_{2g} Raman continuum is crucial as it has an origin of the spinon excitation in the kagome QSL from the theoretical perspective[60]. In the XY configuration for the E_{2g} channel, the Raman tensor on the kagome lattice is written in terms of spin-pair operators[39,60,65,66]

$$\tau_R \propto \sum_R \mathbf{S}_{R3} \cdot (\mathbf{S}_{R1} + \mathbf{S}_{R+\mathbf{a}_2 1} - \mathbf{S}_{R2} - \mathbf{S}_{R-\mathbf{a}_1+\mathbf{a}_2 2}), \quad (2)$$

where $\mathbf{S}_{R1,2,3}$ are spin operators on three sites of the R-th kagome unit cell and $\mathbf{a}_{1,2}$ are the lattice vectors. The spin operator has the spinon $f_{i\sigma}$ representation $S_i^\alpha = \sum_{\sigma\sigma'} f_{i\sigma}^\dagger \tau_{\sigma\sigma'}^\alpha f_{i\sigma'}/2$ where τ^α is the α-th Pauli matrix. The spin-pair is $\mathbf{S}_i \cdot \mathbf{S}_j = -\frac{1}{2}\hat{\chi}_{ij}^\dagger \hat{\chi}_{ij}$ with $\hat{\chi}_{ij} = \sum_\sigma f_{i\sigma}^\dagger f_{j\sigma}$. In the mean field theory, the spinon hopping amplitude $\chi = \langle \hat{\chi}_{ij} \rangle$ is non-zero. So we have 1P and 2P components in the Raman tensor[60]

$$\tau_R^{1P} \propto \chi \sum_R (\hat{\chi}_{R3,R1} + \mathrm{h.c.}) + \cdots, \quad (3)$$

$$\tau_R^{2P} \propto \sum_R \hat{\chi}_{R3,R1}^\dagger \hat{\chi}_{R3,R1} + \cdots, \quad (4)$$

where $\cdots$ denotes omitted terms in Eq. (2) for the notation simplicity. While the 2P component is analogous to the 2M scattering, the 1P contribution is a unique prediction for spinon excitations in the kagome QSL. In Fig. 3d, we schematically decompose the E_{2g} Raman continuum into 1P and 2P components of spinon–antispinon excitations. The 1P component has the maximum at 150 cm^{-1} (1.4J), and extends up to 400 cm^{-1} (3.8J) at low temperatures. The 2P component has the maximum at 400 cm^{-1} (3.8J) and the cut-off around 750 cm^{-1} (6.7J). The mentioned features (maxima and cut-offs) of 1P and 2P excitations in the E_{2g} Raman response agree well with the theoretical prediction for the kagome QSL state[60].

In more detail, the 1P component dominates the E_{2g} magnetic Raman continuum at low frequency. It displays the power-law behavior up to 70 cm^{-1}, with a significantly nonmonotonic temperature dependence, as shown in Fig. 4. The low-energy

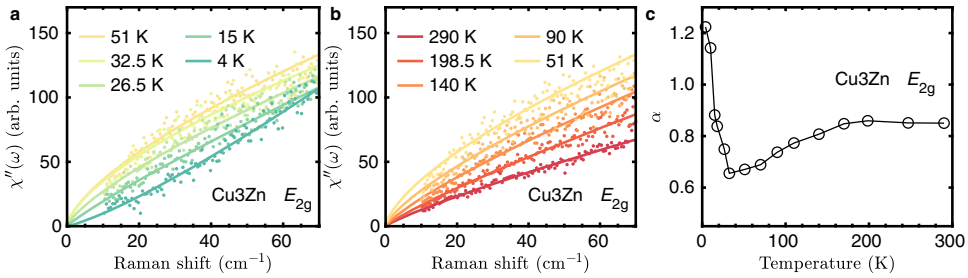

Fig. 4 Power-law behavior for E_{2g} magnetic Raman continua at low frequency in Cu_3Zn. a, **b** are power-law fitting of $\chi''_{E_{2g}}(\omega) \propto \omega^{\alpha}$ at low and high temperatures, respectively. **c** Temperature-dependent exponent α for the power-law fitting.

continuum evolves from a sublinear behavior T^{α} with $\alpha < 1$ to a superlinear one T^{α} with $\alpha > 1$ as reducing the temperature. A central question for the kagome QSL is whether a spin gap exists. Previous results on the powder samples of Cu_3Zn suggest a small spin gap[30,32]. If such a gap exists, the power-law behavior of the E_{2g} magnetic Raman continua sets an upper bound for the spin gap of 2 meV.

The theoretical calculation for kagome Dirac spin liquid (DSL) predicts the power-law behavior for the Raman susceptibility in the E_{2g} channel at low frequency[60]. The 1P spinon excitation in DSL gives the linear density of state (DOS) $\mathcal{D}_{1P} \propto \omega$. The matrix element turns out to be exactly zero for all 1P excitations with $\omega = 0$ in the mean field Dirac Hamiltonian. As a result a Raman spectrum that scales as ω^3 was predicted. However, the vanishing of the matrix element is somewhat accidental and depends on the assumption of a DSL in an ideal kagome Heisenberg model. Any deviation from the ideal DSL state, e.g., a small gap in the ground state[30,32], DM interactions, or other effects of perturbations[26,67], changes the wave functions and may result in a constant matrix element. In that case, the Raman spectrum will be simply proportional to the DOS of the 1P component $\mathcal{D}_{1P}$ which is linear in ω. From our fitting for Cu_3Zn in Fig. 4, we find that $\alpha = 1.3$ when approaching zero temperature. The existence of a small gap in the spinon spectrum may explain the discrepancy.

Considering the interlayer Cu^{2+} concentration (18%) in Cu_3Zn, we make a remark here about the disorder effect in the magnetic Raman scattering. The temperature-dependent E_{2g} static magnetic susceptibility $\chi'_{E_{2g}}(T)$ of Cu_3Zn in Fig. 3 exhibit the maximal spin fluctuations at 50 K. The non-monotonic T-dependence deviating from the Curie–Weiss behavior is associated with the enhancement of nearest-neighbor spin correlations at low temperatures[67]. However, such significant deviation from Curie–Weiss behavior is masked by the interlayer Cu^{2+} moments in the bulk thermodynamic measurements, e.g., heat capacity and bulk magnetization[30]. In contrast to a significant energy dependent magnetic Raman susceptibility $\chi''_{E_{2g}}(\omega)$ at 4 K in Cu_3Zn, the scattered neutron signal $\chi''_{\mathrm{INS}}(\omega)$ in Herbertsmithite is overall insensitive to energy transfer, rather flat above 1.5 meV, but increases significantly with reducing energy below 1.5 meV due to the interlayer Cu^{2+} ions[20,22]. So Raman scattering singles out the kagome magnetic excitations and remains unmasked in the presence of the interlayer Cu^{2+} due to the matrix element effect as explained below. The Raman scattering measures the nearest-neighbor spin-pair $\tau_R \propto \mathbf{S}_i \cdot \mathbf{S}_j$ dynamics, but the spin pairs associated with the interlayer Cu^{2+} ions are weaker than the singlet pairs for the kagome spins. As the light polarization in our Raman measurements is in the kagome ab plane, and the projected factor of the spin-pairs associated with the interlayer Cu^{2+} ions, $(\mathbf{r}_{ij} \cdot \hat{\mathbf{e}}_{\mathrm{in}})(\mathbf{r}_{ij} \cdot \hat{\mathbf{e}}_{\mathrm{out}})$, is small, as the related pair bond vector $\mathbf{r}_{ij}$ has the angle around 52° with respect to the kagome plane. As a result, the interlayer Cu^{2+} ions contribute a negligible Raman matrix element and we ignore their effect in the discussions about the Raman experiments. Moreover, the inelastic neutron scattering in Herbertsmithite measures the magnetic continuum up to $3J$[20], the same energy range as the 1P Raman component in Cu_3Zn. These results suggest that the magnetic Raman continuum originates from the kagome spins, and the 1P component has an origin of spinon excitations.

Figure 5 presents a control Raman study on the magnetic ordered kagome antiferromagnet $EuCu_3$, which has the antiferromagnetic superexchange strength $J \simeq 7$ meV. In Supplementary Note 7, the ARPR scattering on $EuCu_3$ confirms the threefold rotational symmetry. Above the ordering temperature $T_N = 17$ K, the magnetic Raman continuum in the E_g channel displays the extended continuum, similar to the E_{2g} magnetic continuum at 4 K in Cu_3Zn. Below T_N, a sharp peak, i.e., 1M peak as discussed below, is observed on top of the magnetic continuum. The integrated Raman susceptibility $\chi'_{E_g}(T)$ monotonically increases as lowering the temperature as shown in Fig. 5b, different from non-monotonic behavior in $\chi'_{E_{2g}}(T)$ of Cu_3Zn in Fig. 3e. The magnetic Raman susceptibility $\chi''(\omega, T)$ in $EuCu_3$ distributes the main spectral weight among the frequency region less than 400 cm^{-1}, and the magnon peak locates at 72 cm^{-1} below 17 K, as shown in Fig. 5c.

To directly compare the 1P spinon continuum in Cu_3Zn and the 1M peak in $EuCu_3$, we plot the E_g Raman response in $EuCu_3$ at selected temperatures in Fig. 6. The E_{2g} Raman continuum in Cu_3Zn at 4 K is also plotted with the proper scale for the Raman frequency. Above $T_N = 17$ K, $EuCu_3$ has the substantial magnetic continuum with the profile similar to that in Cu_3Zn at 4 K. There are less pronounced low-energy continuum excitations in $EuCu_3$ than those in Cu_3Zn, probably due to the large DM interaction which suppresses the low-energy quantum fluctuations. Below T_N, a sharp magnon peak at 72 cm^{-1} appears in $EuCu_3$ with the corresponding energy scale of the 1P continuum maximum in Cu_3Zn. We stress that the magnon Raman peak is direct spectroscopic evidence for the $\mathbf{q} = 0$ 120° non-collinear AFM spin configurations, and invisible in the $\sqrt{3} \times \sqrt{3}$ structure of the 120° AFM ("Methods").

For the AFM order state, the low-energy excitation is the spin-wave magnon which can be described in the spin-wave theory[68]. In the local spin basis $\tilde{\mathbf{S}}_i$ of the AFM order, we have the Raman tensors in the XY configuration of the E_g channel for 1M and 2M components as following

$$\tau_R^{1M} \propto \sum_R (\tilde{\mathbf{S}}^y_{R1} + \tilde{\mathbf{S}}^y_{R2} - \tilde{\mathbf{S}}^y_{R3}), \tag{5}$$

$$\tau_R^{2M} \propto \sum_R \tilde{\mathbf{S}}_{R3} \odot (\tilde{\mathbf{S}}_{R1} + \tilde{\mathbf{S}}_{R+\mathbf{a}_2 1} - \tilde{\mathbf{S}}_{R2} - \tilde{\mathbf{S}}_{R-\mathbf{a}_1+\mathbf{a}_2 2}), \tag{6}$$

with the 2M spin-pair operator $\tilde{\mathbf{S}}_i \odot \tilde{\mathbf{S}}_j = \tilde{S}^x_i \tilde{S}^x_j + (\tilde{S}^y_i \tilde{S}^y_j + \tilde{S}^z_i \tilde{S}^z_j)/2$. For the details, please refer to the "Methods" section. Therefore, the E_g Raman scattering in the AFM order state measures 1M and 2M excitations as demonstrated in Fig. 1. Thus, the magnon

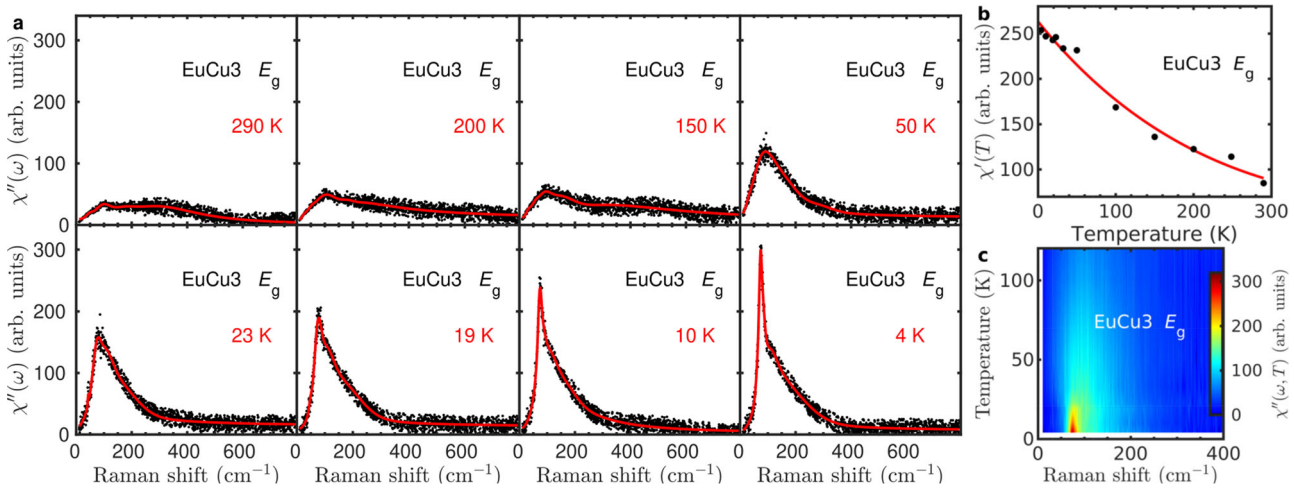

Fig. 5 Temperature dependent E_g magnetic Raman continua in $EuCu_3$. **a** The E_g Raman susceptibility $\chi''_{E_g} = \chi''_{XY}$. The solid lines are guides to the eye. A sharp magnon peak appears in the E_g magnetic Raman continuum below the magnetic transition temperature $T_N = 17$ K. **b** Temperature dependence of the static Raman susceptibility in the E_g channel $\chi'_{E_g}(T) = \frac{2}{\pi}\int_{10\,\mathrm{cm}^{-1}}^{780\,\mathrm{cm}^{-1}} \frac{\chi''_{E_g}(\omega,T)}{\omega} d\omega$. The solid line is a guide to the eye. **c** Color map of $\chi''_{E_g}(\omega, T)$.

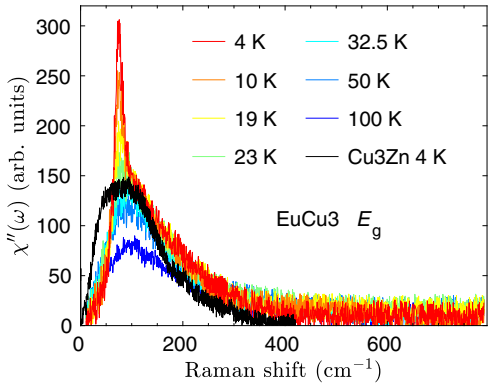

Fig. 6 Comparative Raman studies of $EuCu_3$ and Cu_3Zn. We select the E_g magnetic Raman continua in $EuCu_3$ at several temperatures. For a comparison, we also plot the E_{2g} magnetic Raman continuum in Cu_3Zn at 4 K with the Raman shift scaled by the superexchange energy ratio of 1.9.

excitation emerges from the 1P continuum and can be regarded as the bound state of the spinon–antispinon excitations.

Discussion

Deconfined spinons yield to the magnetic continuum, however, the Raman continuum does not necessarily imply the spin fractionalization. Only 2M excitation itself gives rise to a Raman continuum in the ordered antiferromagnet[42]. In this work, the comparative Raman study in Cu_3Zn and $EuCu_3$ resolves this uncertainty. Guided by the theoretical prediction[60], the E_{2g} Raman continuum can be decomposed into 1P and 2P components of the spinon–antispinon excitations. While the 2P component has the maximum at 3.8J, resembling the 2M broad peak[42], the 1P continuum in Raman is unique for QSL. Its maximum and extended range have the same energy scale as the spin-wave magnon peak in $EuCu_3$ and the inelastic neutron continuum cutoff (up to 3J) in the Herbertsmithite, respectively.

The 1P component of Raman continuum reveals fractionalized spin excitations, providing strong evidence for the kagome QSL ground state in Cu_3Zn. Our comparative Raman studies explicitly show the evolution from the deconfined spinon excitation in the kagome quantum spin liquid compound Cu_3Zn to the conventional magnon in the kagome ordered antiferromagnet $EuCu_3$. On the material side, Zn-Barlowite is an ideal structural realization of the kagome lattice. Along with Herbertsmithite, the single-crystalline Zn-Barlowite stands able to single out the intrinsic properties of the kagome QSL.

Methods

Sample preparation and characterization. High qualified single crystals of Zn-Barlowite was grown by a hydrothermal method similar to crystal growth of herbertsmithite[69,70]. CuO (0.6 g), $ZnBr_2$ (3 g), and NH_4F (0.5 g) and 18 ml deionized water were sealed in a quartz tube and heated between 200 °C and 140 °C by a two-zone furnace. After 3 months, we obtained millimeter-sized single crystal samples. The value of x in $Cu_{4-x}Zn_x(OH)_6FBr$ has been determined as 0.82 by Inductively Coupled Plasma-Atomic Emission Spectroscopy (ICP-AES). The single-crystal X-ray diffraction has been carried out at room temperature by using Cu source radiation ($\lambda = 1.54178$ Å) and solved by the Olex2.PC suite programs[71]. The structure and cell parameters of $Cu_{4-x}Zn_x(OH)_6FBr$ are in coincidence with the previous report on polycrystalline samples[30,32]. For Barlowite($Cu_4(OH)_6FBr$), the mixture of CuO (0.6 g), $MgBr_2$ (1.2 g), and NH_4F (0.5 g) was transferred into Teflon-lined autoclave with 10 ml water. The autoclave was heated up to 260 °C and cooled to 140 °C after 2 weeks. A similar growth condition to Barlowite was applied for the growth of $EuCu_3(OH)_6Cl_3$ with staring materials of $EuCl_3 \cdot 6H_2O$ (2 g) and CuO (0.6 g).

Measurement methods. Our thermodynamical measurements were carried out on the Physical Properties Measurement System (PPMS, Quantum Design) and the Magnetic Property Measurement System (MPMS3, Quantum Design).

The temperature-dependent Raman spectra are measured in a backscattering geometry using a home-modified Jobin-Yvon HR800 Raman system equipped with an electron-multiplying charged-coupled detector (CCD) and a ×50 objective with long working distance and numerical aperture of 0.45. The laser excitation wavelength is 514 nm from an Ar^+ laser. The laser-plasma lines are removed using a BragGrate bandpass filter (OptiGrate Corp.), while the Rayleigh line is suppressed using three BragGrate notch filters (BNFs) with an optical density 4 and a spectral bandwidth ~ 5–10 cm^{-1} [72]. Thus, Raman signal down to 5 cm^{-1} can be measured[73]. The 1800 lines/mm grating enables each CCD pixel to cover 0.6 cm^{-1}. The samples are cooled down to 30 K using a Montana cryostat system under a vacuum of 0.4 mTorr and down to 4 K using an attoDRY 1000 cryogenic system. All the measurements are performed with a laser power below 1 mW to avoid sample heating. The temperature is calibrated by the Stokes-anti-Stokes relation for the magnetic Raman continuum and phonon peaks. The intensities in two cryostat systems are matched by the Raman susceptibility. The ARPR measurements[40] with light polarized in the ab kagome plane of samples were performed in parallel (XX), perpendicular (XY), and X-only polarization configurations (Supplementary Note 5).

SHG measurements were performed using a homemade confocal microscope in a backscattering geometry. A fundamental wave centered at 800 nm was used as excitation source, which was generated from a Ti-sapphire oscillator (Chameleon Ultra II) with an 80 MHz repetition frequency and a 150 fs pulse width. After passing through a ×50 objective, the pump beam was focused on the sample with a diameter of 2 μm. The scattering SHG signals at 400 nm were collected by the same objective and led to the entrance slit of a spectrometer equipped with a

thermoelectrically cooled CCD. Two shortpass filters were employed to cut the fundamental wave.

Magnon Raman peak in kagome AFM ordered state. With a large DM interaction D, the kagome antiferromagnet in Eq. (1) devoleps a $\mathbf{q}=0$ type 120° AFM order at low temperature in $EuCu_3$[53–55,57–59]. In terms of the local basis for the AFM order, we rewrite the Hamiltonian as

$$H = J\sum_{\langle ij\rangle}\tilde{\mathbf{S}}_i\odot\tilde{\mathbf{S}}_j + D\sum_{\langle ij\rangle}\tilde{\mathbf{S}}_i\otimes\tilde{\mathbf{S}}_j, \tag{7}$$

with

$$\tilde{\mathbf{S}}_i\odot\tilde{\mathbf{S}}_j = S_i^xS_j^x + \cos(\theta_{ij})(S_i^yS_j^y + S_i^zS_j^z) + \sin(\theta_{ij})(S_i^zS_j^y - S_i^yS_j^z), \tag{8}$$

$$\tilde{\mathbf{S}}_i\otimes\tilde{\mathbf{S}}_j = \sin(\theta_{ij})(S_i^yS_j^y + S_i^zS_j^z) + \cos(\theta_{ij})(S_i^yS_j^z - S_i^zS_j^y), \tag{9}$$

where θ_{ij} is an angle between two neighboring spins and $S_i^{x,y,z}$ below denotes the local basis of the AFM order. The effective linear spin wave Hamiltonian is given as

$$\mathcal{H}_{\text{eff}} = J\sum_{\langle ij\rangle}[S_i^xS_j^x + (\cos\theta_{ij} + \sin\theta_{ij}D/J)\times(S_i^yS_j^y + S_i^zS_j^z)], \tag{10}$$

for which the Holstein-Primakoff representation for spin operators in the local basis was applied and the energy dispersion was obtained in ref. [68].

In the local spin basis, we have the Raman tensor in the XY configuration is given as

$$\tau_R^{\text{XY}} = \frac{\sqrt{3}}{4}\sum_R\tilde{\mathbf{S}}_{R3}\odot(\tilde{\mathbf{S}}_{R1} + \tilde{\mathbf{S}}_{R+\mathbf{a}_21} - \tilde{\mathbf{S}}_{R2} - \tilde{\mathbf{S}}_{R-\mathbf{a}_1+\mathbf{a}_22}). \tag{11}$$

In the spin-pair operator $\tilde{\mathbf{S}}_i\odot\tilde{\mathbf{S}}_j$ in Eq. (8), there are two-magnon contribution in terms of $S_i^xS_j^x + \cos(\theta_{ij})(S_i^yS_j^y + S_i^zS_j^z)$, and one- and three-magnon contributions in terms of $\sin(\theta_{ij})(S_i^zS_j^y - S_i^yS_j^z)$. For the $\mathbf{q}=0$ spin configuration, we find that τ_R^{XY} in Eq. (11) has the non-vanished one magnon contributions. For the $\sqrt{3}\times\sqrt{3}$ AFM state, τ_R^{XY} has no one-magnon contribution. Therefore, the observed one-magnon peak in the E_g channel in $EuCu_3$ provides evidence for the $\mathbf{q}=0$ spin ordering at low temperatures. In the linear spin-wave theory, we take S^z in the local basis as a constant, $S_i^z = \langle S^z\rangle = 1/2$, and the Raman tensor in XY configuration is given as

$$\tau_R^{\text{XY}} = \frac{3}{8}\sum_R(S_{R1}^y + S_{R2}^y - 2S_{R3}^y), \tag{12}$$

in terms of the local basis, directly measuring the one magnon excitation.

For $EuCu_3$, the exchange interaction parameters are estimated as $J=7$ meV, $D/J=0.3$, leading to the magnon peak position of $\Delta_{sw}=1.1J=77\ \text{cm}^{-1}$, very close to the measured value $72\ \text{cm}^{-1}$ in our Raman measurement of the one-magnon peak.

Data availability

All data supporting the findings of this study are available from the corresponding authors upon reasonable request.

Received: 15 December 2020; Accepted: 6 April 2021;
Published online: 24 May 2021

References

1. Anderson, P. W. Resonating valence bonds: a new kind of insulator? *Mater. Res. Bull.* **8**, 153 (1973).
2. Anderson, P. W. The resonating valence bond state in La_2CuO_4 and superconductivity. *Science* **235**, 1196 (1987).
3. Lee, P. A. An end to the drought of quantum spin liquids. *Science* **321**, 1306 (2008).
4. Balents, L. Spin liquids in frustrated magnets. *Nature* **464**, 199 (2010).
5. Zhou, Y., Kanoda, K. & Ng, T.-K. Quantum spin liquid states. *Rev. Mod. Phys.* **89**, 025003 (2017).
6. Broholm, C. et al. Quantum spin liquids. *Science* **367**, eaay0668 (2020).
7. Kitaev, A. Anyons in an exactly solved model and beyond. *Ann. Phys.* **321**, 2 (2006).
8. Levin, M. & Wen, X.-G. Detecting topological order in a ground state wave function. *Phys. Rev. Lett.* **96**, 110405 (2006).
9. Wen, X.-G. Choreographed entanglement dances: topological states of quantum matter. *Science* **363**, eaal3099 (2019).
10. Ran, Y., Hermele, M., Lee, P. A. & Wen, X.-G. Projected-wave-function study of the spin-1/2 heisenberg model on the kagomé lattice. *Phys. Rev. Lett.* **98**, 117205 (2007).
11. Hermele, M., Ran, Y., Lee, P. A. & Wen, X.-G. Properties of an algebraic spin liquid on the kagome lattice. *Phys. Rev. B* **77**, 224413 (2008).
12. Yan, S., Huse, D. A. & White, S. R. Spin-liquid ground state of the $S=1/2$ Kagome Heisenberg antiferromagnet. *Science* **332**, 1173 (2011).
13. Jiang, H.-C., Wang, Z. & Balents, L. Identifying topological order by entanglement entropy. *Nat. Phys* **8**, 902 (2012).
14. Zaletel, M. P. & Vishwanath, A. Constraints on topological order in mott insulators. *Phys. Rev. Lett.* **114**, 077201 (2015).
15. Mei, J.-W., Chen, J.-Y., He, H. & Wen, X.-G. Gapped spin liquid with $\mathbb{Z}_2$ topological order for the kagome Heisenberg model. *Phys. Rev. B* **95**, 235107 (2017).
16. Norman, M. R. Colloquium: Herbertsmithite and the search for the quantum spin liquid. *Rev. Mod. Phys.* **88**, 041002 (2016).
17. Shores, M. P., Nytko, E. A., Bartlett, B. M. & Nocera, D. G. A structurally perfect $S=1/2$ kagome antiferromagnet. *J. Am. Chem. Soc.* **127**, 13462 (2005).
18. Mendels, P. et al. Quantum magnetism in the paratacamite family: towards an ideal kagomé lattice. *Phys. Rev. Lett.* **98**, 077204 (2007).
19. Wulferding, D. et al. Interplay of thermal and quantum spin fluctuations in the kagome lattice compound herbertsmithite. *Phys. Rev. B* **82**, 144412 (2010).
20. Han, T.-H. et al. Fractionalized excitations in the spin-liquid state of a kagome-lattice antiferromagnet. *Nature* **492**, 406 (2012).
21. Fu, M., Imai, T., Han, T.-H. & Lee, Y. S. Evidence for a gapped spin-liquid ground state in a kagome heisenberg antiferromagnet. *Science* **350**, 655 (2015).
22. Han, T.-H. et al. Correlated impurities and intrinsic spin-liquid physics in the kagome material herbertsmithite. *Phys. Rev. B* **94**, 060409 (2016).
23. Khuntia, P. et al. Gapless ground state in the archetypal quantum kagome antiferromagnet $ZnCu_3(OH)_6Cl_2$. *Nat. Phys.* **16**, 469 (2020).
24. Zorko, A. et al. Symmetry reduction in the quantum kagome antiferromagnet herbertsmithite. *Phys. Rev. Lett.* **118**, 017202 (2017).
25. Laurita, N. J. et al. Evidence for a parity broken monoclinic ground state in the S = 1/2 kagomé antiferromagnet herbertsmithite. Preprint at https://arxiv.org/abs/1910.13606 (2019).
26. Norman, M. R., Laurita, N. J. & Hsieh, D. Valence bond phases of herbertsmithite and related copper kagome materials. *Phys. Rev. Res.* **2**, 013055 (2020).
27. Li, Y. et al. Lattice dynamics in the spin-$\frac{1}{2}$ frustrated kagome compound herbertsmithite. *Phys. Rev. B* **101**, 161115 (2020).
28. Han, T.-H., Singleton, J. & Schlueter, J. A. Barlowite: a spin-1/2 antiferromagnet with a geometrically perfect kagome motif. *Phys. Rev. Lett.* **113**, 227203 (2014).
29. Liu, Z., Zou, X., Mei, J.-W. & Liu, F. Selectively doping barlowite for quantum spin liquid: a first-principles study. *Phys. Rev. B* **92**, 220102 (2015).
30. Feng, Z. et al. Gapped spin-1/2 spinon excitations in a new kagome quantum spin liquid compound $Cu_3Zn(OH)_6$ FBr. *Chinese Phys. Lett.* **34**, 077502 (2017).
31. Feng, Z. et al. Effect of Zn doping on the antiferromagnetism in kagome $Cu_{4-x}Zn_x(OH)_6FBr$. *Phys. Rev. B* **98**, 155127 (2018).
32. Wei, Y. et al. Evidence for a Z_2 topological ordered quantum spin liquid in a kagome-lattice antiferromagnet. Preprint at https://arxiv.org/abs/1710.02991 (2017).
33. Henderson, A. et al. Order-disorder transition in the $S=\frac{1}{2}$ kagome antiferromagnets claringbullite and barlowite. *Chem. Commun.* **55**, 11587 (2019).
34. Pasco, C. et al. Single-crystal growth of Cu_4 $(OH)_6$ BrF and universal behavior in quantum spin liquid candidates synthetic barlowite and herbertsmithite. *Phys. Rev. Mater.* **2**, 044406 (2018).
35. Smaha, R. W., He, W., Sheckelton, J. P., Wen, J. & Lee, Y. S. Synthesis-dependent properties of barlowite and Zn-substituted barlowite. *J. Solid State Chem.* **268**, 123 (2018).
36. Smaha, R. W. et al. Materializing rival ground states in the barlowite family of kagome magnets: quantum spin liquid, spin ordered, and valence bond crystal states. *npj Quantum Mater.* **5**, 1 (2020).
37. Tustain, K. et al. From magnetic order to quantum disorder in the Zn-barlowite series of $S=\frac{1}{2}$ kagomé antiferromagnets. *npj Quantum Mater.* **5**, 74 (2020).
38. Wei, Y. et al. Magnetic phase diagram of $Cu_{4-x}Zn_x(OH)_6FBr$ studied by neutron-diffraction and μSR techniques. *Chinese Phys. Lett.* **37**, 107503 (2020).
39. Cépas, O., Haerter, J. O. & Lhuillier, C. Detection of weak emergent broken-symmetries of the kagome antiferromagnet by Raman spectroscopy. *Phys. Rev. B* **77**, 172406 (2008).
40. Liu, X.-L., Zhang, X., Lin, M.-L. & Tan, P.-H. Different angle-resolved polarization configurations of raman spectroscopy: A case on the basal and edge plane of two-dimensional materials. *Chin. Phys. B* **26**, 067802 (2017).
41. Lemmens, P., Güntherodt, G. & Gros, C. Magnetic light scattering in low-dimensional quantum spin systems. *Physics Reports* **375**, 1 (2003).
42. Devereaux, T. P. & Hackl, R. Inelastic light scattering from correlated electrons. *Rev. Mod. Phys.* **79**, 175 (2007).

43. Wulferding, D., Choi, Y., Lee, W. & Choi, K.-Y. Raman spectroscopic diagnostic of quantum spin liquids. *J. Phys. Condens. Mat.* **32**, 043001 (2019).
44. Sandilands, L. J., Tian, Y., Plumb, K. W., Kim, Y.-J. & Burch, K. S. Scattering continuum and possible fractionalized excitations in α -$RuCl_3$. *Phys. Rev. Lett.* **114**, 147201 (2015).
45. Glamazda, A., Lemmens, P., Do, S. H., Choi, Y. S. & Choi, K. Y. Raman spectroscopic signature of fractionalized excitations in the harmonic-honeycomb iridates β - and γ -Li_2 IrO_3. *Nat. Commun.* **7**, 12286 (2016).
46. Glamazda, A., Lemmens, P., Do, S. H., Kwon, Y. S. & Choi, K. Y. Relation between Kitaev magnetism and structure in α -$RuCl_3$. *Phys. Rev. B* **95**, 174429 (2017).
47. Li, G. et al. Raman spectroscopy evidence for dimerization and Mott collapse in α -$RuCl_3$ under pressures. *Phys. Rev. Mater.* **3**, 023601 (2019).
48. Pei, S. et al. Magnetic Raman continuum in single-crystalline H_3 $LiIr_2$ O_6. *Phys. Rev. B* **101**, 201101 (2020).
49. Wulferding, D. et al. Magnon bound states versus anyonic Majorana excitations in the Kitaev honeycomb magnet α -$RuCl_3$. *Nat. Commun.* **11**, 1603 (2020).
50. Wang, Y. et al. The range of non-Kitaev terms and fractional particles in α -$RuCl_3$. *npj Quantum Mater.* **5**, 14 (2020).
51. Sun, W., Huang, Y.-X., Nokhrin, S., Pan, Y. & Mi, J.-X. Perfect Kagomé lattices in $YCu_3(OH)_6$ Cl_3 : a new candidate for the quantum spin liquid state. *J. Mater. Chem.* **4**, 8772 (2016).
52. Sun, W., Huang, Y. X., Pan, Y. & Mi, J. X. Strong spin frustration and negative magnetization in $LnCu_3(OH)_6$ Cl_3 (Ln=Nd and Sm) with triangular lattices: the effects of lanthanides. *Dalton Trans.* **46**, 9535 (2017).
53. Puphal, P., Zoch, K. M., Désor, J., Bolte, M. & Krellner, C. Kagome quantum spin systems in the atacamite family. *Phys. Rev. Mater.* **2**, 063402 (2018).
54. Zorko, A. et al. Negative-vector-chirality 120° spin structure in the defect- and distortion-free quantum kagome antiferromagnet $YCu_3(OH)_6Cl_3$. *Phys. Rev. B* **100**, 144420 (2019).
55. Arh, T. et al. Origin of magnetic ordering in a structurally perfect quantum kagome antiferromagnet. *Phys. Rev. Lett.* **125**, 027203 (2020).
56. Zorko, A. et al. Dzyaloshinsky-Moriya anisotropy in the spin-1/2 kagome compound $ZnCu_3(OH)_6$ Cl_2. *Phys. Rev. Lett.* **101**, 026405 (2008).
57. Cépas, O., Fong, C. M., Leung, P. W. & Lhuillier, C. Quantum phase transition induced by Dzyaloshinskii-Moriya interactions in the kagome antiferromagnet. *Phys. Rev. B* **78**, 140405 (2008).
58. Rousochatzakis, I., Manmana, S. R., Läuchli, A. M., Normand, B. & Mila, F. Dzyaloshinskii-Moriya anisotropy and nonmagnetic impurities in the $s = \frac{1}{2}$ kagome system $ZnCu_3(OH)_6Cl_2$. *Phys. Rev. B* **79**, 214415 (2009).
59. Zhu, W., Gong, S.-S. & Sheng, D. N. Identifying spinon excitations from dynamic structure factor of spin-1/2 Heisenberg antiferromagnet on the Kagome lattice. *Proc. Natl. Acad. Sci. U.S.* **116**, 5437 (2019).
60. Ko, W.-H., Liu, Z.-X., Ng, T.-K. & Lee, P. A. Raman signature of the U(1) Dirac spin-liquid state in the spin-$\frac{1}{2}$ kagome system. *Phys. Rev. B* **81**, 024414 (2010).
61. Freedman, D. E. et al. Site specific X-ray anomalous dispersion of the geometrically frustrated KAGomé magnet, herbertsmithite, $ZnCu_3(OH)_6$ Cl_2. *J. Am. Chem. Soc.* **132**, 16185 (2010).
62. Helton, J. S. et al. Spin dynamics of the spin-1/2 kagome lattice antiferromagnet $ZnCu_3(OH)_6Cl_2$. *Phys. Rev. Lett.* **98**, 107204 (2007).
63. Halley, J. W. Light scattering as a probe of dynamical critical properties of antiferromagnets. *Phys. Rev. Lett.* **41**, 1605 (1978).
64. Reiter, G. F. Light scattering from energy fluctuations in magnetic insulators. *Phys. Rev. B* **13**, 169 (1976).
65. Fleury, P. A. & Loudon, R. Scattering of light by one- and two-Magnon excitations. *Phys. Rev.* **166**, 514 (1968).
66. Shastry, B. S. & Shraiman, B. I. Theory of Raman scattering in Mott-Hubbard systems. *Phys. Rev. Lett.* **65**, 1068 (1990).
67. Bernu, B., Pierre, L., Essafi, K. & Messio, L. Effect of perturbations on the kagome $S = \frac{1}{2}$ antiferromagnet at all temperatures. *Phys. Rev. B* **101**, 140403 (2020).
68. Chernyshev, A. L. & Zhitomirsky, M. E. Quantum selection of order in an *XXZ* antiferromagnet on a kagome lattice. *Phys. Rev. Lett.* **113**, 237202 (2014).
69. Chu, S., Müller, P., Nocera, D. G. & Lee, Y. S. Hydrothermal growth of single crystals of the quantum magnets: Clinoatacamite, paratacamite, and herbertsmithite. *Appl. Phys. Lett.* **98**, 092508 (2011).
70. Velázquez, M. et al. Aqueous solution growth at 200 °C and characterizations of pure, ^{17}O-or D-based herbertsmithite Zn_xCu_{4-x} $(OH)_6$ Cl_2 single crystals. *J. Cryst. Growth* **531**, 125372 (2020).
71. Dolomanov, O. V., Bourhis, L. J., Gildea, R. J., Howard, J. A. & Puschmann, H. Olex2: a complete structure solution, refinement and analysis program. *J. Appl. Crystallogr.* **42**, 339 (2009).
72. Tan, P. H. et al. The shear mode of multilayer graphene. *Nat. Mater.* **11**, 294 (2012).
73. Lin, M.-L. et al. Cross-dimensional electron-phonon coupling in van der Waals heterostructures. *Nat. Commun.* **10**, 2419 (2019).

Acknowledgements

This work was supported by the National Key Research and Development Program of China (2016YFA0301204), the program for Guangdong Introducing Innovative and Entrepreneurial Teams (No. 2017ZT07C062), by Shenzhen Key Laboratory of Advanced Quantum Functional Materials and Devices (No. ZDSYS20190902092905285), Guangdong Natural Science Foundation (No. 2020B1515120100) and by National Natural Science Foundation of China (Grant Nos. 11774143, 12004377 and 11874350), the CAS Key Research Program of Frontier Sciences (ZDBS-LY-SLH004) and China Postdoctoral Science Foundation (2019TQ0317 and 2020M682780). P.A. Lee acknowledges support by the US Department of Energy under grant number DE-FG02-03ER46076.

Author contributions

J.W.M. conceived the project. P.H.T. conceived the experimental work of Raman spectroscopy. Y.F., L.W., L.H., W.J., and Z.H. synthesized single crystals of samples. M.L. and P.H.T. designed the Raman experiments. M.L., J.Z., and P.H.T. performed Raman measurements. Q.L. and J.D. performed the SHG measurements. Y.F., L.W., L.H., and C.L. performed and analyzed magnetic susceptibility and heat capacity measurements. H.Z., X.S., and J.W.M. performed first-principles calculations. J.W.M., Y.F., M.L., and P.H.T. analyzed the Raman data. P.A.L., J.W.M., and F.Y. worked on the theory. P.A.L., J.W.M., F.Y., P.H.T., and M.L.L. wrote the manuscript with contributions and comments from all authors.

Competing interests

The authors declare no competing interests.

Additional information

Supplementary information The online version contains supplementary material available at https://doi.org/10.1038/s41467-021-23381-9.

Correspondence and requests for materials should be addressed to P.-H.T. or J.-W.M.

Peer review information *Nature Communications* thanks the anonymous reviewers for their contribution to the peer review of this work. Peer reviewer reports are available.

Supplementary Information: Dynamic fingerprint of fractionalized excitations in single-crystalline $Cu_3Zn(OH)_6FBr$

Ying Fu,[1,*] Miao-Ling Lin,[2,3,*] Le Wang,[1] Qiye Liu,[1] Lianglong Huang,[1] Wenrui Jiang,[1] Zhanyang Hao,[1] Cai Liu,[1] Hu Zhang,[4] Xingqiang Shi,[4] Jun Zhang,[2,3,5] Junfeng Dai,[1] Dapeng Yu,[1] Fei Ye,[1,6] Patrick A. Lee,[7] Ping-Heng Tan,[2,3,5,†] and Jia-Wei Mei[1,6,‡]

[1]*Shenzhen Institute for Quantum Science and Engineering, and Department of Physics, Southern University of Science and Technology, Shenzhen 518055, China*
[2]*State Key Laboratory of Superlattices and Microstructures, Institute of Semiconductors, Chinese Academy of Sciences, Beijing 100083, China*
[3]*Center of Materials Science and Optoelectronics Engineering & CAS Center of Excellence in Topological Quantum Computation, University of Chinese Academy of Sciences, 100049 Beijing, China*
[4]*College of Physics Science and Technology, Hebei University, Baoding 071002, China*
[5]*Beijing Academy of Quantum Information Science, Beijing 100193, China*
[6]*Shenzhen Key Laboratory of Advanced Quantum Functional Materials and Devices, Southern University of Science and Technology, Shenzhen 518055, China*
[7]*Department of Physics, Massachusetts Institute of Technology, Cambridge, Massachusetts 02139, USA*
(Dated: April 3, 2021)

CONTENTS

* These two authors contributed equally.
† phtan@semi.ac.cn
‡ meijw@sustech.edu.cn

Supplementary Note 1. ESTIMATION OF EXCHANGE PARAMETERS IN THE KAGOME COMPOUNDS

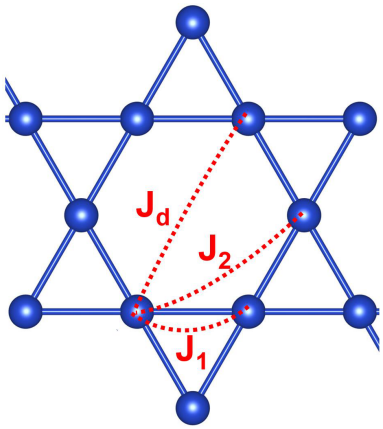

Supplementary Figure 1. Exchange interactions J_1, J_2, and J_d in the Kagome lattice.

We implement the density functional theory (DFT) [1] to estimate the exchange parameters in the kagome compounds. We performed first-principles calculations with the Perdew–Burke–Ernzerhoff revised for solids (PBEsol) functional in generalized gradient approximation (GGA) [2, 3] as implemented in the Vienna Ab Initio Simulation Package (VASP).[4–6] An energy cutoff of 620 eV was used. We used $6 \times 6 \times 4$ Monkhorst-Pack grids [7] for all calculations. All results were obtained with Cu $3d$ valence electrons psudopotential within GGA+U (U_{3d}= 6 eV) scheme.[8]

We fix the lattice constants and relax the atomic positions with a coplanar magnetic structure with negative vector spin chirality in the presence of spin-orbit couplings in our calculations. Exchange interactions can be determined from total energies of various different spin configurations. To determine J_1, J_2, and J_d (see Supplementary Fig. 1), we used the ferromagnetic state, antiferromagnetic state ($\mathbf{q} = 0$), cuboc2 state, and cuboc1 state for a $2 \times 2 \times 1$ supercell as discussed in Fig. 4 of Ref. [9]. Inter-layer couplings J_c are determined by comparing the energies for different stacking patterns of spin configurations. Note for the above interaction terms, we turn off the spin-orbit coupling in our simulations. For the Dzyaloshinski-Moriya (DM) interaction, we turn on spin-orbit couplings and compare the energies of $\mathbf{q} = 0$ antiferromagnetic states with positive and negative vector spin chiralities. The results are listed in Supplementary Table. 1. The nearest neighbor interactions in Cu3Zn and EuCu3 are larger than the experimental values.

Supplementary Table 1. Theoretical results of exchange interaction (in meV) and Cu-O-Cu bonding angle for various materials with the kagome structure. SG denotes the space group. J_c denotes the inter-layer coupling. The references for the lattice constants are also listed.

Formula	SG	J_1 (meV)	J_2 (meV)	J_d (meV)	J_c (meV)	DM (meV)	DM/J_1	∠Cu-O-Cu (∘)	Reference
$Cu_3Zn(OH)_6FBr$	$P6_3/mmc$	24.13	-0.01	-0.65	1.442	1.12	0.05	117.47	[10]
$YCu_3(OH)_6Cl_3$	$P\bar{3}m1$	10.21	0.12	-0.09	0.040	3.45	0.3	118.60	[11]
$EuCu_3(OH)_6Cl_3$	$P\bar{3}m1$	13.02	0.16	-0.08	0.003	3.83	0.3	120.33	[12]
$SmCu_3(OH)_6Cl_3$	$P\bar{3}m1$	13.55	0.14	-0.08	-0.004	5.91	0.4	120.36	[13]

Supplementary Note 2. CRYSTAL PHOTOGRAPH AND THERMODYNAMIC CHARACTERIZATION

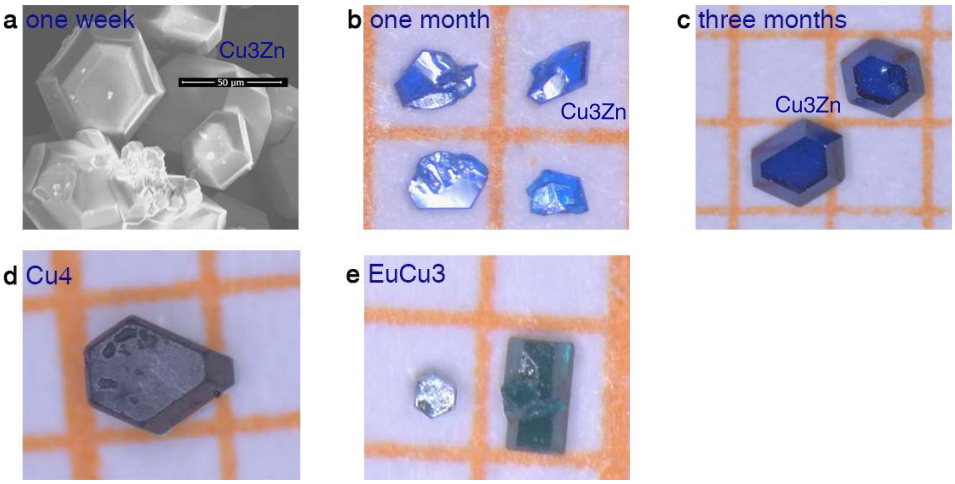

Supplementary Figure 2. Photographs for single crystals of Cu3Zn, Cu4 and EuCu3. Crystal sizes and morphologies of $Cu_3Zn(OH)_6FBr$ (Cu3Zn) for different growth periods: (a) one weak, (b) one month, and (c) three months. (d) $Cu_4(OH)_6FBr$ (Cu4); (e) $EuCu_3(OH)_6Cl_3$ (EuCu3). The yellow grid in (b), (c), (d) and (e) is 1×1 mm^2.

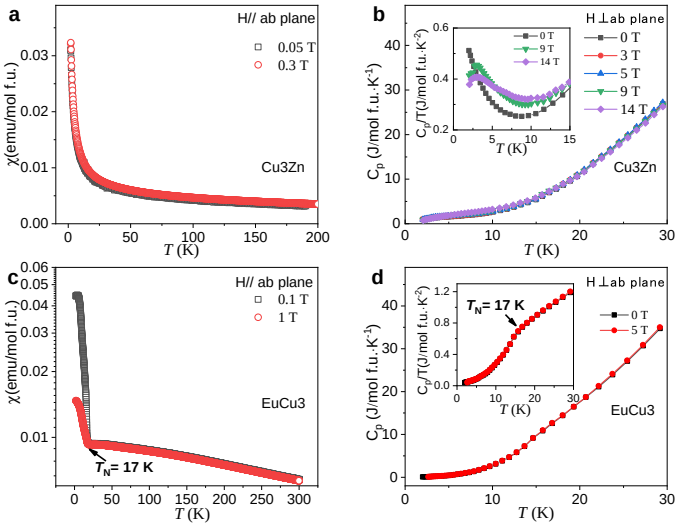

Supplementary Figure 3. Thermodynamic properties of single crystals for Cu3Zn and EuCu3. (a) Temperature dependent magnetic susceptibilities ($\chi = M/H$) at 0.05 T and 0.3 T fields. (b) The temperature dependent specific heat C_p at different magnetic fields in Cu3Zn. The thermodynamic properties of single crystals for Cu3Zn agree well with previous results on the powder samples.[10, 14] (c) The magnetic susceptibilities show the ordering temperature $T_N = 17$ K in EuCu3. The Eu^{3+} with ground state of $^7F_0$ contributes to the Van Vleck paramagnetism (d) The temperature dependent heat capacities C_p in EuCu3.

Supplementary Note 3. TEMPERATURE EVOLUTION OF THE RAMAN SPECTRA AND PHONON MODE ASSIGNMENT IN Cu3Zn

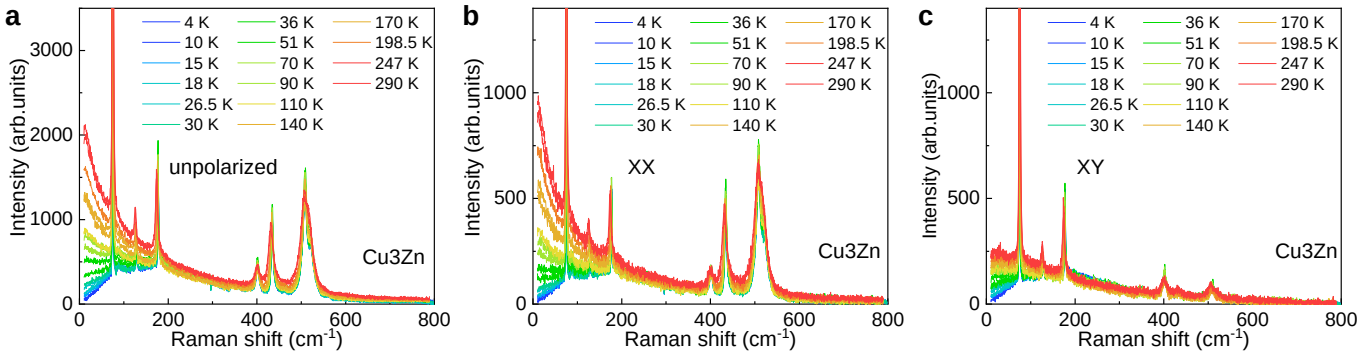

Supplementary Figure 4. Raman spectra in Cu3Zn at different temperatures. (a) Unpolarized Raman spectra in Cu3Zn. (b) Raman spectra in the XX configuration contain the A_{1g} and E_{2g} channel. (c) Raman spectra in the XY configuration contain the E_{2g} channel.

Supplementary Table 2. Phonon mode assignment for Cu3Zn. Cu3Zn crystallizes the space group $P6_3/mmc$ (No. 194) and has Raman-active A_{1g}, E_{1g}, and E_{2g} modes according to the point group representation of D_{6h} $(6/mmm)$. E_{1g} is not visible when the light polarization lies in the kagome ab plane, and we have Raman-active phonon modes $\Gamma_{\text{Raman}} = 4A_{1g} + 9E_{2g}$.

Frequency (Exp.) (cm^{-1})	Modes (Exp.)	Frequency (Cal.) (cm^{-1})	Modes (Cal.)	Associated vibrating irons
74.6	E_{2g}	71.2	E_{2g}	Br^-
126.4	E_{2g}	124.11	E_{2g}	Zn^{2+}
172.2	E_{2g}	184.18	E_{2g}	F^-
355.5	E_{2g}	345.37	E_{2g}	O^{2-}
401.5	E_{2g}	396.21	E_{2g}	O^{2-}
430.8	A_{1g}	426.06	A_{1g}	O^{2-}
488.6	E_{2g}, visible in 532 nm	493.47	E_{2g}	O^{2-}
521.1	A_{1g}	508.84	A_{1g}	O^{2-}
920.3	E_{2g}	920.33	E_{2g}	H^+
1016.7	A_{1g}	1082.26	A_{1g}	H^+
1028.2	E_{2g}, weak	1020.11	E_{2g}	H^+
3352.3	?	3333.19	E_{2g}	H^+
3467.5	A_{1g}	3512.14	A_{1g}	H^+

Supplementary Note 4. RAMAN SPECTRA EVOLUTION FROM Cu4 TO Cu3Zn AND FANO EFFECT IN Cu3Zn

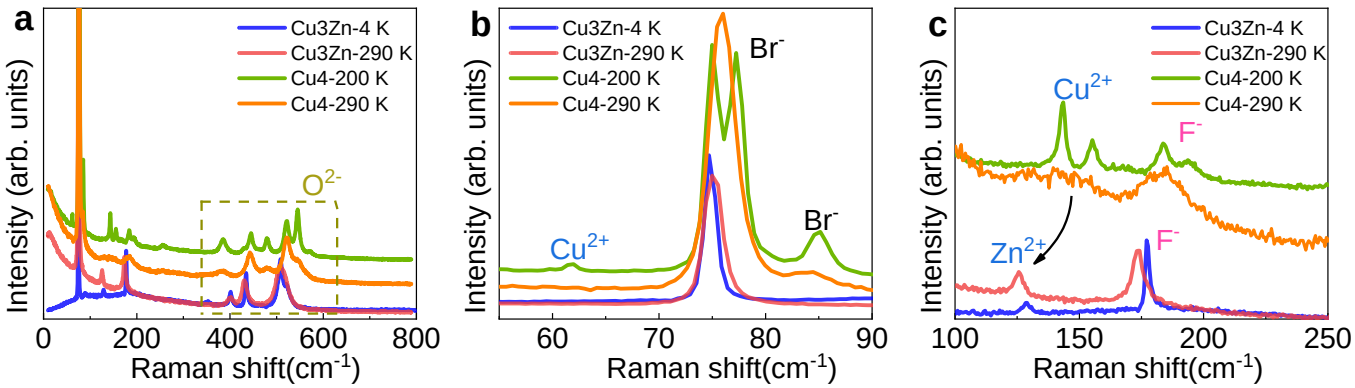

Supplementary Figure 5. Raman spectral evolution from Cu4 to Cu3Zn. (a) Unpolarized Raman spectra for Cu4 and Cu3Zn at selected temperatures. Comparison for phonon modes between 40 cm^{-1} and 90 cm^{-1} in (b), and between 100 cm^{-1} and 250 cm^{-1} in (c) for Cu4 and Cu3Zn. The Cu4 spectra in (a), (b) and (c) have been offset vertically for clarity. The phonon evolution from Cu4 to Cu3Zn displays the difference by substituting the interlayer Cu^{2+} site of Cu4 with Zn^{2+} in Cu3Zn. The parent Barlowite Cu4 transforms to orthorhombic *Pnma* below $T \approx 265$ K, characterized by changes in the relative occupancies of the interlayer Cu^{2+} site. Between 300 cm^{-1} and 600 cm^{-1}, there are several phonon peaks associated with O^{2-} vibrations in Cu4 and Cu3Zn. Cu3Zn displays the in-plane relative vibration of Br^{-} (E_{2g} mode) at 75 cm^{-1}, and has no Raman-active mode related to the kagome Cu^{2+} vibrations since Cu^{2+} is the inversion center. The Br^{-} phonon mode splits into two peaks in Cu4 due to the superlattice folding in the orthorhombic Pnma phase at low temperature. An additional Br^{-} peak at 85 cm^{-1} appears in Cu4, related to the Br vibrations along the c-axis. The kagome layers in Cu4 are distorted at low temperature, signaled by a new phonon mode for the kagome Cu^{2+} vibration at 62 cm^{-1}. Cu3Zn displays sharp E_{2g} modes at 125 cm^{-1} and 173 cm^{-1} corresponding to in-plane relative movements for Zn^{2+} and F^{-}, respectively. The corresponding modes (interlayer Cu^{2+} and F^{-} vibrations) in Cu4 are broad at 290 K due to the randomly distributed interlayer Cu^{2+} and split into two peaks at 200 K.

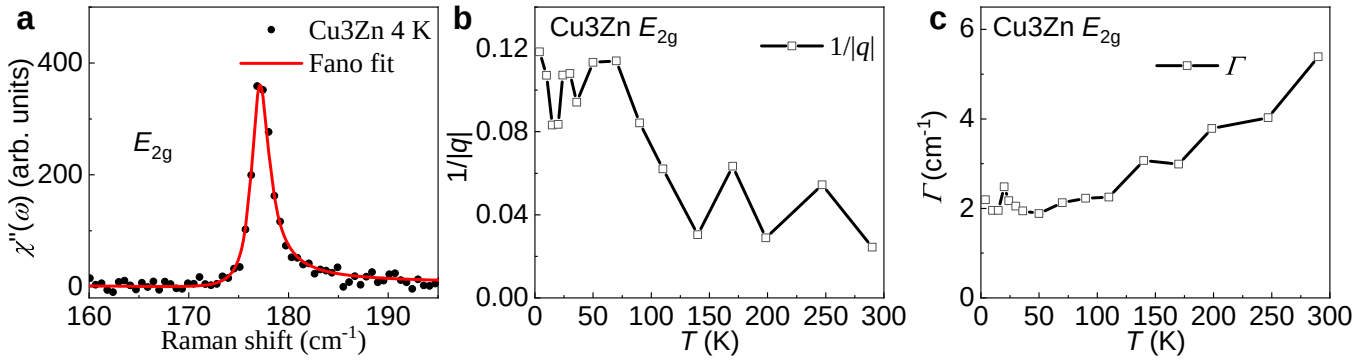

Supplementary Figure 6. Fano lineshape of the E_{2g} F^{-} phonon peak at 173 cm^{-1} in Cu3Zn. (a) Fano lineshape for the E_{2g} in-plane phonon mode related to F atomic movement. Temperature dependent Fano asymmetric parameter $1/|q|$ in (b) and the width Γ in (c). The asymmetric Fano lineshape provides an additional probe of the magnetic degree of freedom.

Supplementary Note 5. LIGHT POLARIZATION CONFIGURATIONS IN ANGLE-RESOLVED POLARIZED RAMAN SCATTERING

The polarized Raman measurements with light polarized in the ab kagome plane of samples were performed in parallel (XX), perpendicular (XY), and X-only polarization configurations. Two typical polarization configurations were utilized to measure the angle-resolved polarized Raman (ARPR) spectra: i) a half-wave plate was put after the polarizer in the incident path to vary the angles between the polarization of incident laser and the analyzer with the fixed vertical polarization, which can be denoted as the X-only configuration; ii) a half-wave plate is allocated in the common path of the incident and scattered light to simultaneously vary their polarization directions, while the polarizations of incident laser and analyzer were parallel or perpendicular to each other. By rotating the fast axis of the half-wave plate with an angle of $\theta/2$, the polarization of incident and/or scattered light is rotated by θ.

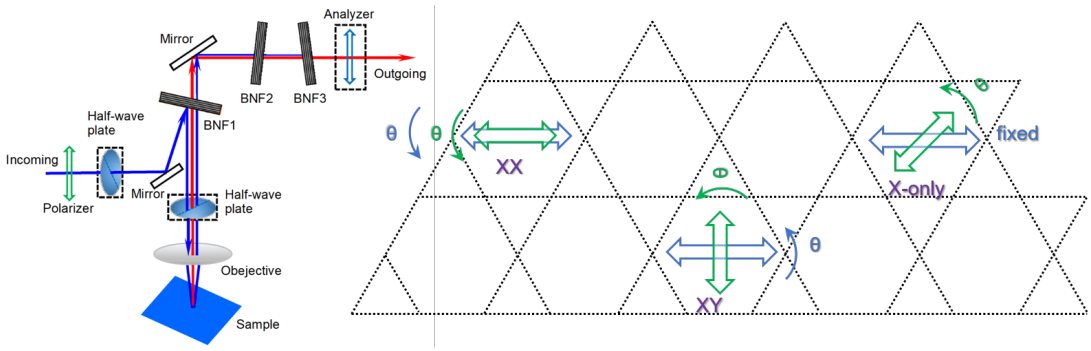

Supplementary Figure 7. Three polarization configurations in the ARPR response. In the XX (XY) configuration, the incoming and outgoing light polarizations are parallel (perpendicular) and we rotate both of them simultaneously. In the X-only configuration, the outgoing light polarization is fixed and we rotate the incoming light polarization only.

Supplementary Note 6. SECOND-HARMONIC-GENERATION (SHG) RESULTS OF Cu3Zn

SHG measurements were performed using a homemade confocal microscope in a back-scattering geometry. A fundamental wave centered at 800 nm was used as excitation source, which was generated from a Ti-sapphire oscillator (Chameleon Ultra II) with an 80 MHz repetition frequency and a 150 fs pulse width. After passing through a 50× objective, the pump beam was focused on the sample with a diameter of 2 μm. The scattering SHG signals at 400 nm were collected by the same objective and led to the entrance slit of a spectrometer equipped with a thermoelectrically cooled CCD. Two shortpass filters were employed to cut the fundamental wave.

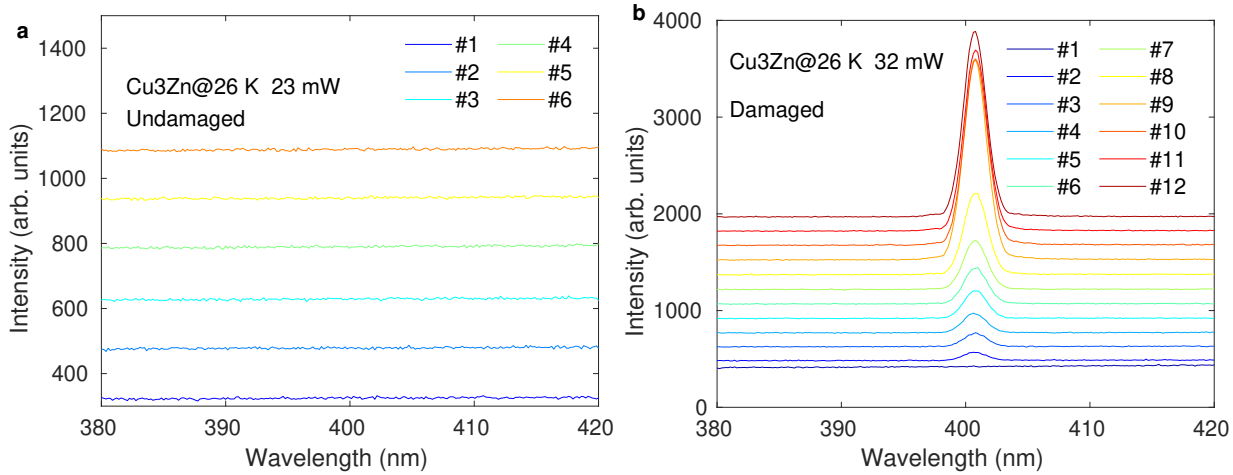

Supplementary Figure 8. SHG in Cu3Zn at 26 K with different laser powers. (a) SHG measurements in the same spot of sample taken every 5 seconds (from #1 to #6). At 23 mW, SHG signals in Cu3Zn sample are absent, implying that inversion symmetry remains preserved. (b) A series of SHG measurements under the excitation power of 32 mW in the same point of the sample taken every 5 seconds (from #1 to #12). A remarkable SHG signal at 400 nm is detectable after a 10-second exposure, which dramatically enhances as the time increases. Due to the damage or degradation of Cu3Zn under high power excitation, the inversion symmetry breaking induces a strong SHG signals in sample. By comparison, we conclude that undamaged Cu3Zn single crystal presents spatial inversion symmetry at low temperature. The lines have been offset vertically for clarity.

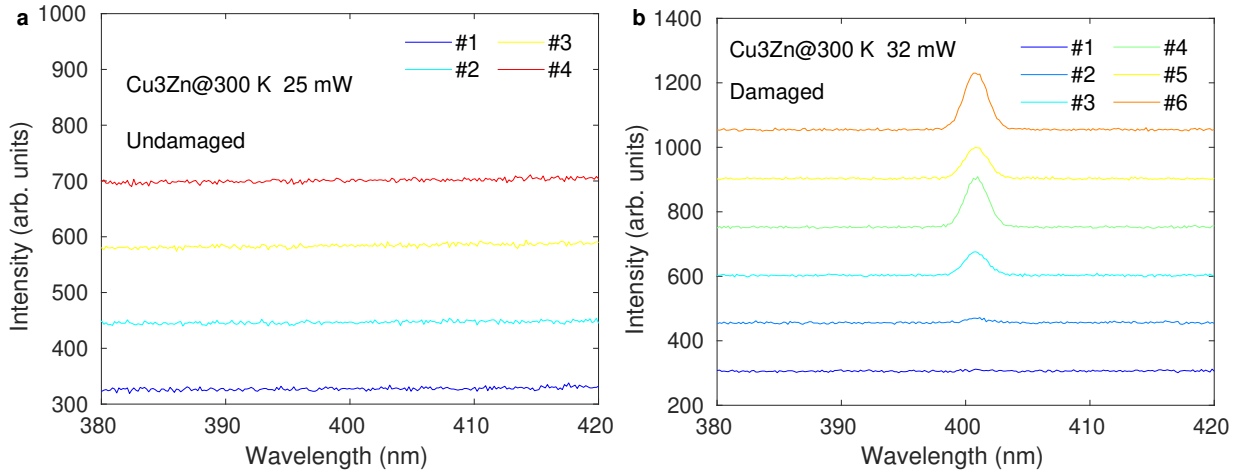

Supplementary Figure 9. SHG in Cu3Zn at 300 K with different laser powers. (a) and (b) represent the successive SHG measurements in the same point of sample taken every 5 seconds with excitation powers at 25 mW and 32 mW, respectively. There are no SHG signals at the excitation power of 25 mW, whereas strong SHG signals appear at the excitation power above 32 mW after a 10-second exposure. By comparison, damage or degradation in crystal structure under high power excitation induces a detectable SHG signal, implying that inversion symmetry presents in undamaged Cu3Zn at room temperature. The lines have been offset vertically for clarity.

Supplementary Note 7. RAMAN RESPONSES IN EuCu3

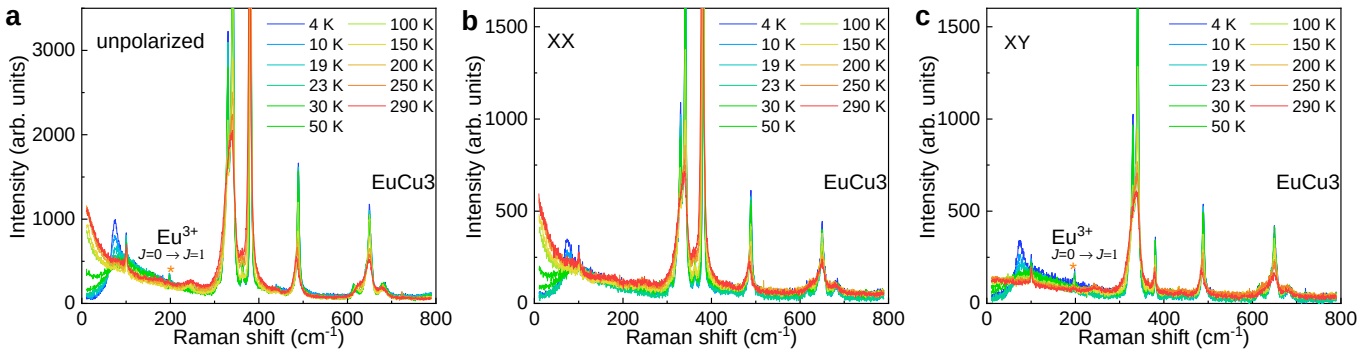

Supplementary Figure 10. Raman spectra of EuCu3 at different temperatures. (a) Unpolarized Raman spectra. (b) Raman spectra in the XX configuration in EuCu3 contain the $A_{\rm g}$ and $E_{\rm g}$ channel. (c) Raman spectra in the XY configuration contain the $E_{\rm g}$ and $A_{2\rm g}$ channel. For Eu^{3+}, we observe the $A_{2\rm g}$ excitation of the $4f^6$ configuration with the transition from ${}^7F_{J=0}$ to ${}^7F_{J=1}$.

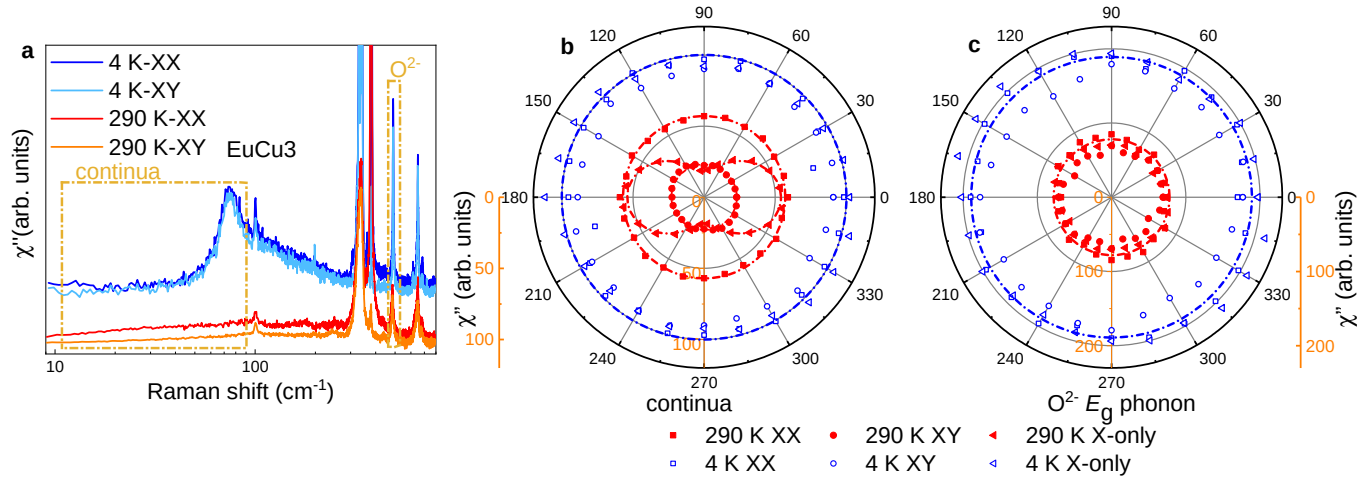

Supplementary Figure 11. Rotation symmetry of Raman dynamics for lattice vibrations and magnetic excitations in EuCu3. We monitor the selected magnetic continuum at low frequency and the O^{2-} $E_{\rm g}$ mode in (a). (b) ARPR dependence of the integrated Raman continuum from 9 to 80 cm^{-1}. The continua at 290 K follow the $\cos^2(\theta)$ function for the $A_{1\rm g}$ channel, while in other cases, the continua remain constant. (c) ARPR dependence of the O^{2-} $E_{\rm g}$ phonon (487 cm^{-1}) scattering intensity. Its Raman intensity is independent of θ.

[1] R. O. Jones, Density functional theory: Its origins, rise to prominence, and future, Rev. Mod. Phys. **87**, 897 (2015).
[2] J. P. Perdew, K. Burke, and M. Ernzerhof, Generalized gradient approximation made simple, Phys. Rev. Lett. **77**, 3865 (1996).
[3] J. P. Perdew, A. Ruzsinszky, G. I. Csonka, O. A. Vydrov, G. E. Scuseria, L. A. Constantin, X. Zhou, and K. Burke, Restoring the density-gradient expansion for exchange in solids and surfaces, Phys. Rev. Lett. **100**, 136406 (2008).
[4] G. Kresse and J. Furthmüller, Efficient iterative schemes for ab initio total-energy calculations using a plane-wave basis set, Phys. Rev. B **54**, 11169 (1996).
[5] M. Gajdoš, K. Hummer, G. Kresse, J. Furthmüller, and F. Bechstedt, Linear optical properties in the projector-augmented wave methodology, Phys. Rev. B **73**, 045112 (2006).
[6] J. Hafner, Ab-initio simulations of materials using vasp: Density-functional theory and beyond, J. Comput. Chem. **29**, 2044 (2008).
[7] H. J. Monkhorst and J. D. Pack, Special points for brillouin-zone integrations, Phys. Rev. B **13**, 5188 (1976).
[8] A. I. Liechtenstein, V. V. Anisimov, and J. Zaanen, Density-functional theory and strong interactions: Orbital ordering in mott-hubbard insulators, Phys. Rev. B **52**, R5467 (1995).
[9] L. Messio, C. Lhuillier, and G. Misguich, Lattice symmetries and regular magnetic orders in classical frustrated antiferromagnets, Phys. Rev. B **83**, 184401 (2011).

[10] Z. Feng, Z. Li, X. Meng, W. Yi, Y. Wei, J. Zhang, Y.-C. Wang, W. Jiang, Z. Liu, S. Li, F. Liu, J. Luo, S. Li, G. qing Zheng, Z. Y. Meng, J.-W. Mei, and Y. Shi, Gapped Spin-1/2 Spinon Excitations in a New Kagome Quantum Spin Liquid Compound $Cu_3Zn(OH)_6FBr$, Chinese Physics Letters **34**, 077502 (2017).

[11] A. Zorko, M. Pregelj, M. Gomilšek, M. Klanjšek, O. Zaharko, W. Sun, and J.-X. Mi, Negative-vector-chirality 120° spin structure in the defect- and distortion-free quantum kagome antiferromagnet $\mathrm{YCu_3(OH)_6Cl_3}$, Phys. Rev. B **100**, 144420 (2019).

[12] P. Puphal, K. M. Zoch, J. Désor, M. Bolte, and C. Krellner, Kagome quantum spin systems in the atacamite family, Phys. Rev. Materials **2**, 063402 (2018).

[13] W. Sun, Y. X. Huang, Y. Pan, and J. X. Mi, Strong spin frustration and negative magnetization in $LnCu_3(OH)_6Cl_3$ (Ln = Nd and Sm) with triangular lattices: the effects of lanthanides, Dalton Trans. **46**, 9535 (2017).

[14] Y. Wei, Z. Feng, W. Lohstroh, C. dela Cruz, W. Yi, Z. F. Ding, J. Zhang, C. Tan, L. Shu, Y.-C. Wang, J. Luo, J.-W. Mei, Z. Y. Meng, Y. Shi, and S. Li, Evidence for a Z_2 topological ordered quantum spin liquid in a kagome-lattice antiferromagnet (2017), arXiv:1710.02991.